

Simultaneous state estimation and attenuation correction for thunderstorms with radar data using an Ensemble Kalman Filter: Tests with simulated data

Ming Xue,^{a,b,*} Mingjing Tong^a and Guifu Zhang^b

^aCenter for Analysis and Prediction of Storms, University of Oklahoma, Norman, Oklahoma, USA

^bSchool of Meteorology, University of Oklahoma, Norman, Oklahoma, USA

ABSTRACT: A new approach to dealing with attenuated radar reflectivity data in the data assimilation process is proposed and tested with simulated data using the ensemble square-root Kalman filter. This approach differs from the traditional method where attenuation is corrected in observation space first before observations are assimilated into numerical models. We build attenuation correction into the data assimilation system by calculating the expected attenuation within the forward observation operators using the estimated atmospheric state. Such a procedure does not require prior assumption about the types of hydrometeor species along the radar beams, and allows us to take advantage of knowledge about the hydrometeors obtained through data assimilation and state estimation. Being based on optimal estimation theory, error and uncertainty information on the observations and prior estimate can be effectively utilized, and additional observed parameters, such as those from polarimetric radar, can potentially be incorporated into the system. Tests with simulated reflectivity data of an X-band 3 cm wavelength radar for a supercell storm show that the attenuation correction procedure is very effective – the analyses obtained using attenuated data are almost as good as those obtained using unattenuated data. The procedure is also robust in the presence of moderate dropsizes-distribution-related observation operator error and when systematic radar calibration error exists. The analysis errors are very large if no attenuation correction is applied. The effect of attenuation and its correction when radial velocity data are also assimilated is discussed as well. In general, attenuation correction is equally important when quality radial velocity data are also assimilated. Copyright © 2009 Royal Meteorological Society

KEY WORDS data assimilation; X-band radar reflectivity

Received 8 June 2008; Revised 18 March 2009; Accepted 1 May 2009

1. Introduction

Compared to 10 cm wavelength S-band weather radars, 3 cm wavelength X-band radars have smaller antennae and lower construction costs. X-band radars are also more suitable for airborne deployment and can be more cost-effectively deployed in high-density networks providing high spatial resolutions. The latter include the experimental X-band networks of CASA (Center for Collaborative Adaptive Sensing of the Atmosphere; McLaughlin *et al.*, 2007), a National Science Foundation Engineering Research Center. The Observing System Simulation Experiments (OSSEs) of Xue *et al.* (2006; hereafter XTD06) using simulated data have shown that the assimilation of additional data from CASA-type radars improves the analysis of a supercell storm. However, in that study, simulated radar data were assumed to be unattenuated. Compared to S-band, attenuation poses an additional challenge at X-band for radar data assimilation and other applications. For example, the specific rain attenuation for a typical X-band radar is about 1 dB

km⁻¹ for a rain rate of 50 mm hr⁻¹, yielding a total two-way attenuation of more than 40 dB over 20 km. To successfully use reflectivity data from X-band radars for quantitative precipitation estimation and storm-scale data assimilation, the effect of attenuation must be properly accounted for. In fact, attenuation correction is a significant area of research in utilizing reflectivity observations from X-band and other shorter-wavelength radars.

Existing attenuation correction techniques include (i) the Hitschfeld and Bordan (H–B) solution/algorithm and its modified versions for correcting single polarization radar reflectivity (Hitschfeld and Bordan, 1954), and (ii) the methods based on differential phase measurement from dual-polarization radar (Jameson, 1992; Bringi and Chandrasekar, 2000). Smyth and Illingworth (1998) utilized the information of negative differential reflectivity (Z_{DR}) on the far side of heavy precipitation for attenuation correction. In addition, dropsizes distribution (DSD) retrieval can be performed using dual-frequency or dual-polarization observations (Meneghini and Liao, 2007) to improve attenuation correction.

The H–B method uses a reflectivity-attenuation relation to solve for true reflectivity from attenuated reflectivity. Its solution is sensitive to error accumulation

*Correspondence to: Dr. Ming Xue, School of Meteorology, University of Oklahoma, NWC Suite 2500, 120 David Boren Blvd, Norman OK 73072, USA.
E-mail: mxue@ou.edu

and the procedure can become unstable when attenuation is large, when an improper relation is used (Johnson and Brandes, 1987) or when systematic error associated with, e.g. radar calibration, exists. The H–B solution can be made stable by using total path-integrated attenuation (PIA) as a constraint; such a method has been applied successfully to the space/air-borne radar measurement of rain in the TRMM project (Meneghini and Kozu, 1990) where the PIA is determined using the surface reference method. Independent estimate of PIA is, however, not available in general. Also, in our case with multiple co-existing species, typical attenuation correction methods, including that of H-B, usually have difficulties.

A dual-polarization radar provides more measurements and, at the same time, more constraints that allow for more reliable attenuation correction. It has been found that the specific differential phase is almost linearly related to specific attenuation (Bringi and Chandrasekar, 2000, section 7.4). Hence, the differential propagation phase is more directly related to PIA and has been used in attenuation correction (Jameson, 1992; Ryzhkov and Zrnich, 1995). The correction is done either by directly adding to reflectivity and differential reflectivity using correction amounts determined from the measured differential propagation phase (Matrosov *et al.*, 2002; Anagnostou *et al.*, 2006) or by adjusting coefficients in the attenuation-reflectivity and attenuation-differential phase relations used in the attenuation correction procedure, such that the system is self consistent (Bringi *et al.*, 2001; Park *et al.*, 2005).

All of the above techniques are applied in observation space, based on directly observed data. Such an approach usually requires prior assumptions about the hydrometeor species and/or their DSDs, especially when polarimetric radar measurements are not available. Even when polarimetric measurements are available, it is difficult for these methods to deal with more than two coexisting hydrometeor species (e.g. rain, snow and hail). The presence of wet ice particles, such as melting or water-coated hail or graupel, can significantly complicate the problem; in such cases, observation-based correction methods often become ineffective. In addition, these traditional methods do not effectively utilize the error or uncertainty information associated with different measurements.

Most past research on attenuation correction has focused on quantitative precipitation estimation, where accurate attenuation correction at higher elevations is less of a concern. In recent years, significant progress has been made in assimilating radar reflectivity data into storm-scale numerical weather prediction (NWP) models (e.g. Xue *et al.*, 2003; Tong and Xue, 2005; Hu *et al.*, 2006a). For this purpose, accurate treatment of attenuation, including the presence of mixed phases, is important at all height levels.

The optimal estimation theory, in which different sources of information together with their error or uncertainty are optimally combined (usually in the least-square sense) to obtain the best estimate of the state and/or parameters, has found applications in many fields. The optimal estimation theory is also the foundation

of modern data assimilation for the atmosphere (Daley, 1991; Kalnay, 2002). The variational technique and the ensemble Kalman filter (EnKF, Evensen 1994) are advanced data assimilation methods based on optimal estimation theory and have been effectively applied to convective-scale model initialization with (S-band) radar data (e.g. Sun and Crook, 1997; Snyder and Zhang, 2003; Tong and Xue, 2005; Hu *et al.*, 2006b).

With variational and EnKF approaches, observations in their original form can be directly used as long as proper forward observation operators to convert the state variables and/or parameters to the observed quantities can be developed. In the case of satellite observations, the observation operators convert atmospheric state variables, including temperature, pressure and water vapour, into observed radiances. For radar, the operators convert the atmospheric state variables, including velocity, temperature, moisture and hydrometeor species and amount, into observed radial velocity, reflectivity, differential reflectivity and phase, as well as other derived parameters. Accurate observational operators should take into account radar beam propagation (e.g. Gao *et al.*, 2006), beam pattern weighting (e.g. Xue *et al.*, 2006, 2007a), thermodynamic effects such as melting (e.g. Jung *et al.*, 2008) and attenuation. Error propagation through the measurement and data processing can be estimated using properly constructed observation operators (Xue *et al.*, 2007b). With proper observation operators, variational and EnKF methods seek to minimize the difference between the observed quantities, which may be attenuated, and the model presentation of those quantities, subject to their respective uncertainties. Information with smaller uncertainty will be weighted more in the minimization/estimation process, and prior estimate together with its uncertainty information can also be readily used.

The variational approach has been employed by Hogan (2007) for estimating rain rate using dual-polarization radar data, where attenuation correction is built directly into the observation operator. Several advantages for using the variational approach for the intended application were quoted in that study. They include the explicit treatment of errors, the straightforward inclusion of attenuation without the instability problem encountered by H–B, the direct use of differential phase shift ϕ_{dp} instead of the usually very noisy specific differential phase K_{dp} , and the ease of building spatial smoothing into the analysis procedure. However, with such standalone analysis procedures, it is difficult to directly couple rain-rate estimation with precipitation microphysics employed in numerical models, assuming the model microphysics is accurate enough to benefit such coupling.

For purpose of data assimilation, an alternative to performing attenuation correction first is to build the attenuation into the observation operators and assimilate the attenuated observations directly. With this approach, attenuation correction is performed simultaneously with the state estimation. Since radar measurements are closely linked to microphysics, a data assimilation method that is capable of dealing with mixed-phase microphysics is most desirable.

EnKF is particularly useful for radar data assimilation, because the flow-dependent background-error covariances derived from the forecast ensemble can be used to ‘retrieve’ state variables not directly observed. Recently, Tong and Xue (2005; TX05 hereafter) show that EnKF is able to accurately ‘retrieve’ microphysical species associated with a mixed-phase microphysics parametrization scheme when assimilating (unattenuated) single-polarization reflectivity data. For these reasons, EnKF is chosen to test simultaneous state estimation and attenuation correction in this study. The Doppler radar considered is assumed to have single polarization, and only the storm environment as defined by a single sounding is assumed known at the beginning of state estimation. Because reflectivity is a function of several hydrometeor species, which themselves are unknown in the beginning, it is not obvious whether simultaneous state estimation and attenuation correction can be successful. As the first study to evaluate the proposed concept, we employ OSSEs that use simulated data. For the general philosophy behind OSSEs, readers are referred to discussions in Lord *et al.* (1997).

The rest of this paper is organized as follows. The attenuation equations together with the equations for equivalent reflectivity factor Z_e and attenuation coefficient k as functions of hydrometeor state are described in section 2. The simulation of attenuated observations using a radar emulator is also described. The experimental set-up and data assimilation configuration are given in section 3. The results of the OSSEs with and without attenuation correction, and additional sensitivity experiments testing the effect of observation operator error and systematic radar calibration error are discussed in section 4. A summary is given in section 5.

2. Reflectivity and attenuation equations and simulation of observations

Microphysics parametrization schemes that predict only a single moment of the hydrometeor DSDs (e.g. Lin *et al.*, 1983; Hong and Lim, 2006) continue to be the schemes most commonly used in both research and operational NWP applications. Such schemes typically assume exponential DSDs with prescribed intercept parameters, and predict the third moment of DSD, the mixing ratios of hydrometeors. Multi-moment microphysics schemes, in which additional prognostic equations are solved to determine certain parameters in the DSD functions, have gained more attention in recent years (e.g. Milbrandt and Yau, 2005, 2006; Dawson *et al.*, 2009). No research has been published so far, however, involving assimilation of radar data using a multi-moment microphysics scheme. In principle, the reflectivity and attenuation formulae are dependent on the DSDs, and in the case of exponential DSD, on the assumed intercept parameters. As initial studies of Tong and Xue (2008a) and Jung *et al.* (2009) have shown, it is possible to perform simultaneous DSD parameter retrieval and state estimation using radar data. In the control set of experiments in this paper, we assume

that the intercept parameters of the hydrometeors are known. We test the effect of DSD uncertainty in a set of sensitivity experiments.

In this section, we present the equations for X-band reflectivity and attenuation, which form part of the forward observation operator for radar reflectivity data. These equations are used in both radar data simulation and assimilation. The relations between equivalent reflectivity factor Z_e , attenuation coefficient k and the state of hydrometeors are derived for each species. These relations, combined with the radar emulator introduced in XTD06 and briefly described here, form the complete forward observation operator.

2.1. The attenuation equation

The measured equivalent reflectivity factor in the presence of attenuation at a given range r can be expressed as

$$Z_e'(r) = Z_e(r)A(r), \quad (1)$$

where $Z_e(r)$ is the equivalent reflectivity factor before attenuation,

$$A(r) = \exp\left(-0.46 \int_0^r k(s) ds\right)$$

is the two-way PIA factor for equivalent reflectivity, and k is the attenuation coefficient (dB km^{-1}). The attenuated reflectivity in dBZ can be obtained by applying $10 \log_{10}(\)$ to Equation (1), so that

$$Z'(r) = Z(r) - 2 \int_0^r k(s) ds, \quad (2)$$

where $Z(r)$ and $Z'(r)$ are reflectivity in dBZ before and after attenuation, i.e. the intrinsic reflectivity and attenuated reflectivity, respectively. It can be seen that the total PIA in dB, i.e. $\text{PIA} = -10 \log_{10} A(r)$, is equal to twice the integral of k between range 0 and r , reflecting the effects of two-way attenuation. For the purpose of data assimilation, the effect of attenuation and its correction can be achieved by including Equation (1) as part of the observation operator for reflectivity. The radar reflectivity factor Z_e and attenuation coefficient k are directly related to the state of the hydrometeors. In the following, we will derive the relations between Z_e , k and the water mass content of hydrometeors.

2.2. Z - W and k - W relations for X-band radar

Z_e and k are linked to hydrometeor mass content (W , in mass per unit volume of air) through DSDs. Consistent with the DSD assumptions in the 5-class single-moment microphysics scheme of Lin *et al.* (1983, hereafter LFO83) used in the prediction model of this study, the DSDs of rain, snow and hail/graupel are assumed to have an exponential form:

$$N(D) = N_0 \exp(-\Lambda D), \quad (3)$$

where N_0 is the intercept parameter and Λ is the slope parameter. The intercept N_0 is a fixed constant, and the slope parameter is then uniquely linked to W ($= \rho_a q$, where ρ_a is air density and q is the mixing ratio), given assumptions about the DSD and hydrometeor density.

The hydrometeor content and radar variables are represented by weighted integrals over the DSDs as follows:

$$W = \frac{\pi}{6} \rho \int D^3 N(D) dD, \quad (4)$$

$$Z_e = \frac{\lambda^4}{\pi^5 |K_W|^2} \int \sigma_b(D) N(D) dD, \quad (5)$$

$$k = 4.343 \int \sigma_e(D) N(D) dD, \quad (6)$$

where ρ is the density of hydrometeors, $K_W = \frac{\epsilon_r - 1}{\epsilon_r + 2}$ is the dielectric factor of water, ϵ_r is the relative dielectric constant of water, σ_b is the backscattering radar cross-section and σ_e the extinction cross-section for hydrometeor particles. The cross-sections are calculated using Mie theory or T-matrix method, depending experiments.

In practice, during data assimilation, we want to avoid direct scattering calculation and integration over DSD for efficiency reasons. Instead, we perform the calculations within the possible range of water content beforehand, and use curve fitting to obtain formulae that can be used efficiently within data assimilation. Because the formulae will be used for every observation assimilated, computational efficiency is important. The alternative is to use look-up tables. The fitted curves are attractive because they can be more easily documented; we use them whenever relatively simple yet accurate enough curves can be obtained.

We derive the parametrized relations between model-predicted W with Z_e and k using the following procedure:

- 1) Use (3) in (4) and solve for Λ as a function of W , yielding the slope parameter $\Lambda = \left(\frac{N_0 \pi \rho}{W}\right)^{1/4}$.
- 2) Let W vary in its possible range and calculate Λ then the corresponding Z_e and k using (5) and (6). The Mie theory or T-matrix method is used to calculate the backscattering radar cross-sections and the attenuation or extinction cross-sections here.
- 3) Performing least-square fitting to the data for Z_e - W and k - W in log domain, leading to power-law relations

$$Z_e = \alpha_Z W^{\beta_Z} \quad \text{and} \quad k = \alpha_k W^{\beta_k}. \quad (7)$$

The units for W , Z_e and k are g m^{-3} , $\text{mm}^6 \text{m}^{-3}$ and dB km^{-1} , respectively. The above procedure is applied to all hydrometeor species and the results are given below.

2.2.1. Rainwater

In this paper, the calculations for Z_e and k in the observation operators within the data assimilation process are based on Equations (7), assuming Mie scattering

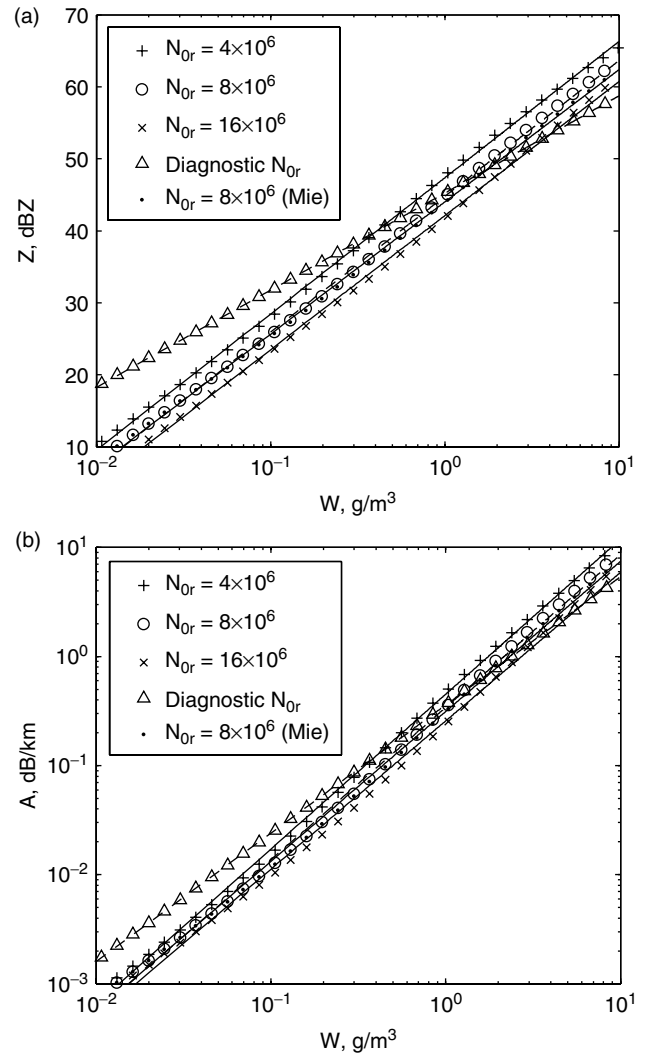


Figure 1. Reflectivity (a) and attenuation (b) as function of rain water content, calculated using T-matrix method for three different values of rain intercept parameter N_{Or} , and for the diagnostic N_{Or} , and those obtained using Mie scattering method for the default value of N_{Or} ($= 8 \times 10^6$). The temperature is assumed to be 10°C . The curves fitted to the data are also plotted.

and a 10°C temperature. The relative dielectric constant used is $\epsilon_r = 55.43 - 37.85i$, a complex number. Rain intercept parameter assumes the default value, $N_{Or} = 8 \times 10^6 \text{ m}^{-4}$, of the Marshall-Palmer DSD used in LFO83. The resulting parameters in (7) are $\alpha_{Zr} = 2.53 \times 10^4$, $\beta_{Zr} = 1.84$, $\alpha_{kr} = 0.319$ and $\beta_{kr} = 1.38$ (Table I) where subscript r denotes rain. The calculations and fitted curves are plotted against water content in Figure 1. The calculated points are almost completely aligned in straight lines in the log-log plot (Z_e and A are in log space), suggesting relations close to the power law.

The reflectivity and attenuation are dependent on the DSD, and on the temperature to a lesser extent. In the above, we assumed spherical rain drop shapes so that the Mie scattering theory can be applied. In a set of sensitivity experiments, we test the effects of DSD uncertainty and of approximating the raindrops as spherical in the assimilation by simulating the observations using different intercept parameter values and using T-matrix

Table I. Coefficients for rain radar reflectivity and attenuation calculations obtained using Mie scattering and T-matrix methods, for different temperatures and different values of rain intercept parameter N_{0r} .

Parameter	T = 0 °C, Mie				T = 0 °C, T-matrix				T = 10 °C, T-matrix				T = 20 °C, T-matrix									
	8 × 10 ⁶	4 × 10 ⁶	8 × 10 ⁶	16 × 10 ⁶	8 × 10 ⁶	4 × 10 ⁶	8 × 10 ⁶	16 × 10 ⁶	4 × 10 ⁶	8 × 10 ⁶	16 × 10 ⁶	4 × 10 ⁶	8 × 10 ⁶	16 × 10 ⁶	4 × 10 ⁶	8 × 10 ⁶	16 × 10 ⁶	4 × 10 ⁶	8 × 10 ⁶	16 × 10 ⁶	DiagN _{0r}	
N_{0r} (m ⁻⁴)	25300	53189	1.877	1.849	16024	32515	1.338	1.342	30021	16190	33399	1.348	1.360	30021	16190	33399	1.348	1.360	30021	16190	33399	34225
α_{Zr}	1.84	1.877	0.446	0.269	1.849	1.338	0.3531	0.257	1.883	1.860	1.348	0.3593	0.257	1.883	1.860	1.348	0.3593	1.902	1.895	1.869	1.869	1.359
β_{Zr}	0.319	0.446	1.368	1.303	0.269	0.3531	1.152	1.360	0.342	0.257	0.3593	1.175	1.360	0.342	0.257	0.3593	1.175	0.4500	0.3321	0.2423	0.2423	0.3586
α_{kr}	1.38	1.368	1.342	1.303	1.303	1.152	1.152	1.360	1.398	1.360	1.175	1.175	1.360	1.398	1.360	1.175	1.175	1.469	1.452	1.411	1.411	1.199
β_{kr}	1.38	1.368	1.342	1.303	1.303	1.152	1.152	1.360	1.398	1.360	1.175	1.175	1.360	1.398	1.360	1.175	1.175	1.469	1.452	1.411	1.411	1.199

(Zhang *et al.*, 2001) scattering calculations to account for non-spherical raindrop shapes. We also examine the effect of temperature.

When using the T-matrix method to calculate the backscattering and extinction cross-sections of raindrops, the mean drop shape is assumed to have an empirically fitted axis ratio following Brandes *et al.* (2002). The water dielectric constant is calculated based on Ray (1972). The calculated and fitted attenuation and reflectivity are plotted in Figure 1 for three different values of N_{0r} that are equal to the default, and twice and half of the default, as well as for diagnostic N_{0r} that is a function of W (Zhang *et al.*, 2008). Table I lists the fitted parameters α_{Zr} , β_{Zr} , α_{kr} , and β_{kr} for 0 °C, 10 °C, and 20 °C temperatures and the four cases of N_{0r} .

The table shows that the sensitivity to temperature of α and β parameters for rainwater is much smaller than to N_{0r} . These parameters change by only a few percent between 0 °C and 20 °C, while α values for Z_e and k differ by a factor of 2 to 3 between N_{0r} values twice and half of the default. There is also some difference between α calculated using the Mie and T-matrix methods for the same temperature but overall Z_e and A calculated using these two different methods are very close (Figure 1). A similar result is true for snow and hail (not shown). Because of the relatively small sensitivity to temperature, we will test the effect of observation operator error in sensitivity experiments by simulating the data using different N_{0r} (as well as N_{0s} and N_{0h}) and of scattering calculation methods while keeping temperature at 10 °C, which is close to the mean temperature of the layer of atmosphere below the freezing level in this case.

It can be shown that the α coefficients are inversely proportional to the intercept parameter, $\alpha_{Zr} \propto N_{0r}^{-(\beta_{Zr}-1)}$ (this is close to the analytical result of Rayleigh scattering of $\alpha_{Zr} \propto N_{0r}^{-0.75}$), and $\alpha_{kr} \propto N_{0r}^{-(\beta_{kr}-1)}$. This is because the larger N_{0r} is, the smaller are the raindrops, and hence the smaller are the reflectivity and attenuation. Again, a similar result is true for snow and hail.

2.2.2. Dry snow and hail

The calculation and fitting procedures for dry hail and dry snow are the same as those for rain. Mie scattering theory is used for hail and snow because they have little polarization signatures. For snow, $N_{0s} = 3 \times 10^6$ m⁻⁴, $\rho_s = 0.1$ g cm⁻³ (s is for snow), and for hail $N_{0h} = 4 \times 10^4$ m⁻⁴, $\rho_h = 0.917$ g cm⁻³ (h is for hail), and they are the default values used in LFO83 scheme. The resultant formulae for dry snow and dry hail are

$$Z_{es} = 3.48 \times 10^3 W_s^{1.66} \text{ (mm}^6 \text{ m}^{-3}\text{)}, \quad (8)$$

$$k_s = 0.00483 W_s^{1.28} \text{ (dB km}^{-1}\text{)}, \quad (9)$$

$$Z_{eh} = 8.18 \times 10^4 W_h^{1.50} \text{ (mm}^6 \text{ m}^{-3}\text{)}, \quad (10)$$

$$k_h = 0.159 W_h^{1.64} \text{ (dB km}^{-1}\text{)}. \quad (11)$$

In the later experiments that use N_{0s} and N_{0h} that are twice or half of the default values, instead of recalculating the α and β values through scattering calculation, we keep

β unchanged (whose dependency on N_0 is small) and set α according to

$$\alpha_{\text{new}} = \alpha_{\text{default}} (N_{0,\text{new}}/N_{0,\text{default}})^{-(\beta-1)}$$

because $\alpha \propto N_0^{-(\beta-1)}$. For the sensitivity experiments, the exact values of α and β are not important (the purpose is to introduce uncertainty to these variables).

2.2.3. Melting snow and hail

The melting ice model of Jung *et al.* (2008) is used to derive the formulae for melting or wet snow and hail. The coefficients are derived as functions of melting percentage f_w , calculated following Equations (2) and (3) of Jung *et al.* (2008). The density of melting snow is also diagnosed from f_w (Equation (4) of Jung *et al.*, 2008). Using the same procedure as above, we can obtain the coefficients for the power-law relations. For wet snow:

$$a_{Zs} = (0.00491 + 5.75 f_{ws} - 5.58 f_{ws}^2) \times 10^5, \quad (12)$$

$$b_{Zs} = 1.67 - 0.202 f_{ws} + 0.398 f_{ws}^2, \quad (13)$$

$$a_{ks} = 0.0413 + 22.7 f_{ws} - 50.5 f_{ws}^2 + 28.6 f_{ws}^3, \quad (14)$$

$$b_{ks} = 1.06 - 0.579 f_{ws} + 2.03 f_{ws}^2 - 1.24 f_{ws}^3, \quad (15)$$

and for wet hail:

$$a_{Zh} = (0.809 + 10.13 f_{wh} - 5.98 f_{wh}^2) \times 10^5, \quad (16)$$

$$b_{Zh} = 1.48 + 0.0448 f_{wh} - 0.0313 f_{wh}^2, \quad (17)$$

$$a_{kh} = 0.256 + 6.28 f_{wh} - 11.36 f_{wh}^2 + 6.01 f_{wh}^3, \quad (18)$$

$$b_{kh} = 1.26 - 0.659 f_{wh} + 1.44 f_{wh}^2 - 0.817 f_{wh}^3. \quad (19)$$

3. OSSE Experiments

3.1. The truth storm simulation

We test our attenuation correction procedure based on the EnKF assimilation system using simulated data for a classic 20 May 1977 Del City, Oklahoma supercell storm case (Ray *et al.*, 1981) through OSSEs (e.g. Lord *et al.*, 1997). In the experiments, radar radial velocity and reflectivity data are sampled from a truth simulation using a radar emulator, which is based on the reflectivity and attenuation formula discussed earlier.

The forecast model used is the Advanced Regional Prediction System (Xue *et al.*, 2000, 2001, 2003). As in TX05, the ARPS is used in a 3D cloud model mode and the prognostic variables include three velocity components u , v , w , potential temperature θ , pressure p , and six categories of water substances, *i.e.* water vapour specific humidity q_v , and mixing ratios for cloud water q_c , rainwater q_r , cloud ice q_i , snow q_s and hail q_h . In addition, turbulence kinetic energy is also predicted which is used to determine turbulent mixing coefficients based on a 1.5-order turbulence closure scheme. The microphysical processes are parametrized using the three-category ice scheme of Lin *et al.* (1983).

As in TX05, for all experiments, the physical model domain is $64 \times 64 \times 16 \text{ km}^3$ in size and has horizontal grid spacing of 2 km and a vertical spacing of 0.5 km. The initially homogeneous storm environment is defined by a modified Del City sounding as used in Xue *et al.* (2001) and the storm is triggered by a 4 K thermal bubble having an ellipsoidal bubble that is centred at $x = 48$, $y = 16$ and $z = 1.5 \text{ km}$, with radii of 10 km in x and y and 1.5 km in the z direction. Open conditions are used at the lateral boundaries. A wave radiation condition is also applied at the top boundary. Free-slip conditions are applied to the bottom boundary. The length of simulation is up to three hours. A constant wind of $u = 3 \text{ m s}^{-1}$ and $v = 14 \text{ m s}^{-1}$ is subtracted from the observed sounding to keep the primary (right-moving) storm cell near the centre of the model grid.

3.2. Simulation of radar observations

An X-band polarimetric radar is assumed to be located at the southwest corner of the model domain with a maximum range large enough to cover the entire storm. The simulation of radar data follows XTD06, using a Gaussian power weighting function in the vertical for observations simulated on radar elevation levels (plan position indicator planes). In the horizontal, the data are assumed to have been interpolated to the model Cartesian coordinates (the horizontal locations of model grid columns). The effects of Earth curvature and beam bending due to vertical change of refractivity are taken into account using the 4/3 effective Earth radius model discussed in Doviak and Zrníc (1993). The velocity is projected to the direction of radar beam locally to give the simulated radial velocity. The radar is assumed to operate in the standard US operational WSR-88D radar precipitation scan mode, having 14 elevations with one volume scan every 5 minutes and a 1° beam width. The attenuated reflectivity is calculated by integrating along the path of each radar beam using Equation (2), where the reflectivity before attenuation (in dBZ) is given by $Z = 10 \log_{10}[Z_{er} + Z_{es} + Z_{ews} + Z_{eh} + Z_{ewh}]$, (where subscripts ws and wh denote wet snow and wet hail, respectively) and the unattenuated equivalent reflectivity for different species are given in section 2.2.

As an example, Figure 2 shows the simulated radar reflectivity (before simulated errors are added) at an elevation of 4.3° with and without attenuation at 70 and 100 min of model time. In the unattenuated fields shown in Figure 2(a) and (c), high reflectivity ($Z > 45 \text{ dBZ}$) is found in the core precipitation regions of the two split cells (called the left and right movers after cell splitting), mainly associated with high mixing ratios of rainwater and hail, including melting hail. The most significant effect of attenuation is found on the far side of high reflectivity regions from the observing radar. As shown in Figure 2(b) and (d), the reflectivity to the northeast of the precipitation core of the right-moving cell (near the centre of the domain) is completely attenuated, resulting in a wedge where no reflectivity is observed. The maximum reflectivity in the core region is reduced by more than 10

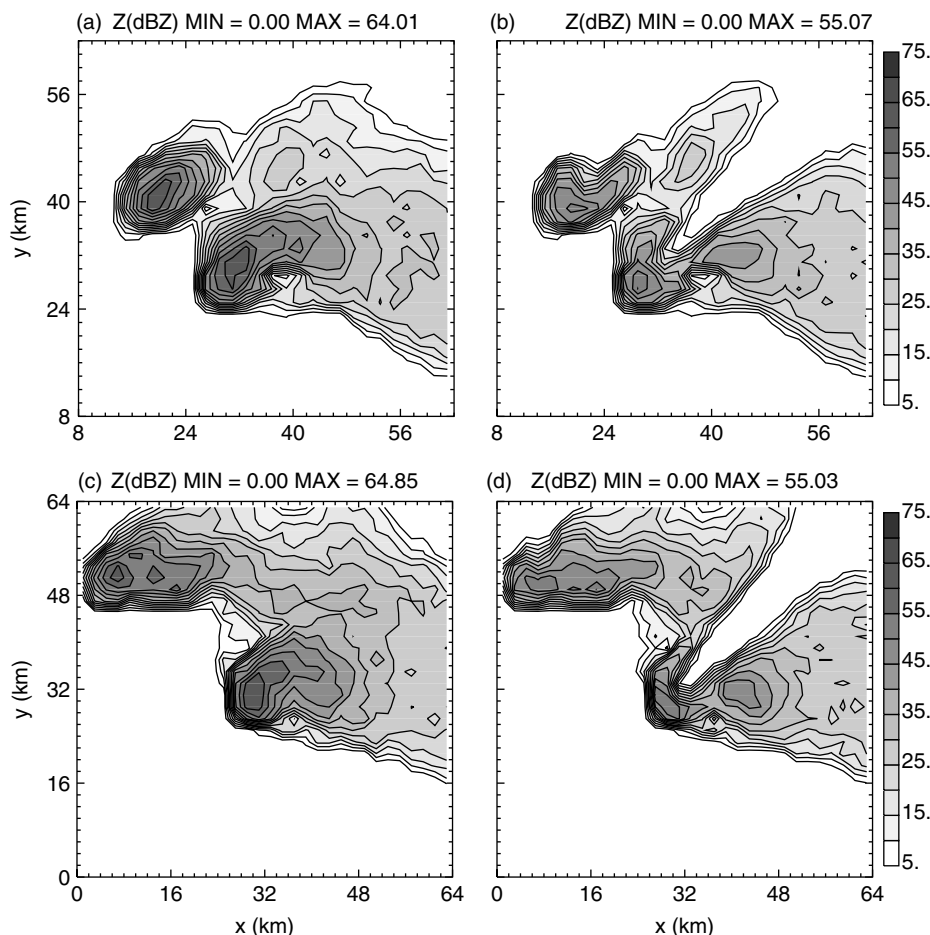


Figure 2. Simulated Z observations at (a, b) 70 and (c, d) 100 minutes of model time at an elevation angle of 4.3° , (a, c) without and (b, d) with attenuation effect in the Z simulation. The radar is located at the lower left corner of the domain.

dBZ. The pattern and magnitude of attenuation appear realistic.

In the standard experiments, Gaussian-distributed random errors of zero mean and 1 m s^{-1} and 2 dB standard deviations, respectively, are added to the simulated radial velocity, V_r , and reflectivity, Z , data sampled from the truth storm simulation. These values are also used to specify the observation error variances during data assimilation, except in some special experiments to be discussed later. In one experiment, additional systematic error representing radar calibration error is introduced into the data to test the robustness of the algorithm in the present of calibration error.

3.3. The EnSRF data assimilation procedure

The EnKF data assimilation algorithm used is based on the ensemble square-root Kalman filter (EnSRF) of Whitaker and Hamill (2002), and the filter configurations follow the control experiment (CNTL) of Tong and Xue (2008b) closely. Following Whitaker and Hamill (2002), the serial EnSRF algorithm for analyzing uncorrelated observations, one after another, is summarized here. With the serial analysis, the observations are analyzed one at a time. Therefore, the observation error covariance matrix \mathbf{R} reduces to a scalar, so does matrix $\mathbf{HP}^b\mathbf{H}^T$, which is the

background-error covariance between observation points. The analysis equations for ensemble mean state vector, $\bar{\mathbf{x}}$, and the ensemble deviation from the mean, \mathbf{x}'_i , are, respectively:

$$\bar{\mathbf{x}}^a = \bar{\mathbf{x}}^b + \mathbf{K}[y_j^o - H(\bar{\mathbf{x}}^b)], \quad (20)$$

$$\mathbf{x}'_i{}^a = \mu(\mathbf{I} - \lambda\mathbf{KH})\mathbf{x}'_i{}^b, \quad (21)$$

where

$$\mathbf{K} = \mathbf{P}^b\mathbf{H}^T(\mathbf{HP}^b\mathbf{H}^T + \mathbf{R})^{-1}, \quad (22)$$

is the Kalman gain matrix, \mathbf{P}^b is the background or prior error covariance matrix, \mathbf{H} is the linearized version of the observation operator that projects state variable \mathbf{x} to the j th observation y_j^o . Here, superscripts a, b and o denote analysis, background and observation, respectively. The ensemble mean analysis, $\bar{\mathbf{x}}^a$, is obtained first from Equation (20), the deviation from the mean by the i th ensemble member is then given by Equation (21), in which μ is a covariance inflation factor that is usually slightly larger than 1, and

$$\lambda = [1 + \sqrt{\mathbf{R}(\mathbf{HP}^b\mathbf{H}^T + \mathbf{R})^{-1}}]^{-1}. \quad (23)$$

Equation (23) is only valid for single observation analysis and therefore both the numerator and denominator

inside the square root are scalars and the evaluation of λ is easy. In the above, the background-error covariances $\mathbf{P}^b\mathbf{H}^T$ and $\mathbf{H}\mathbf{P}^b\mathbf{H}^T$ are estimated from the background ensemble, according to

$$\mathbf{P}^b\mathbf{H}^T = \frac{1}{K-1} \sum_i^K [\mathbf{x}_i^b - \bar{\mathbf{x}}^b][H(\mathbf{x}_i^b) - \overline{H(\mathbf{x}^b)}]^T, \quad (24)$$

$$\mathbf{H}\mathbf{P}^b\mathbf{H}^T = \frac{1}{K-1} \sum_i^K [H(\mathbf{x}_i^b) - \overline{H(\mathbf{x}^b)}][H(\mathbf{x}_i^b) - \overline{H(\mathbf{x}^b)}]^T, \quad (25)$$

where K is the ensemble size, H is the observation operator which can be nonlinear (true for reflectivity). For a single observation, $\mathbf{P}^b\mathbf{H}^T$ is a vector having the length of vector \mathbf{x} and $\mathbf{H}\mathbf{P}^b\mathbf{H}^T$ is a scalar. In practice, because of covariance localization, all elements in $\mathbf{P}^b\mathbf{H}^T$ are not calculated; those outside the influence range of a given observation are assumed to be zero. After the analysis of one observation is completed, the analysis becomes the new background (\mathbf{x}^a becomes \mathbf{x}^b) for the next observation and the analysis is repeated. After all observations at a given time are analyzed, an ensemble of forecasts proceeds from the analysis ensemble until the time of new observation(s), at which time the analysis cycle is repeated.

In our system, the analysis variables contained in state vector \mathbf{x} include the grid point values of u , v , w , θ , p , q_v , q_c , q_r , q_i , q_s and q_h . The observation vector \mathbf{y}^o contains radar radial velocity V_r and reflectivity Z . The observation operator H contains that for attenuated reflectivity Z' given by Equation (2), and that for radial velocity, mapping velocity at the grid points to radial velocity on the radar elevations. Following Tong and Xue (2008b), the terminal velocity effect is explicitly included in the radial velocity observation operator.

Closely following the control experiment of Tong and Xue (2008b), we start the initial ensemble forecast at 20 min of model time when the first storm cell developing out of an initial bubble reaches peak intensity. The ensemble is initialized by adding smoothed random perturbations to a horizontally homogeneous ensemble mean defined by the environmental sounding. The perturbation smoothing procedure is described in Tong and Xue (2008b) and the standard deviations of the smoothed perturbations are, respectively, 2 m s^{-1} for velocity components, 2 K for potential temperature, and 0.6 g kg^{-1} for q_v , q_c , q_r , q_i , q_s and q_h .

Forty ensemble members are used in all experiments. Radar observation volumes are assimilated every 5 min from 25 min to 100 min. The same background-error covariance localization procedure as in Tong and Xue (2008b) is used, with a localization radius of 6 km in all direction. Covariance inflation is not applied for reasons stated in that paper. Briefly, the effect of covariance inflation is small in this case. Additional details on the

assimilation configurations can be found in Tong and Xue (2008b). We point out here that, because the first guess for the first cycle is simply given by the environmental sounding, the initial model state has no idea about the storm. The state of the storm, including that of all microphysical species, must be estimated by the filter, using information contained in (attenuated) radar data.

3.4. Assimilation experiments

Two sets of standard experiments are first performed, one assimilating Z data only and the other assimilating both V_r and Z . Both sets of experiments contain four runs; designated by names starting with one of NA, NAC, NACLE or AC, and ending with either ZV or Z (e.g. NAZV). NA stands for no attenuation and is used to denote runs which assume that the radar data are not attenuated at all and accordingly no attenuation correction is applied. Such cases serve as baselines for comparison. Attenuated radar data are assimilated in experiments whose names start with NAC, NACLE or AC. NAC indicates that attenuation correction is not performed even though the data used are attenuated, while AC denotes that attenuation correction is performed. In experiments starting with NACLE, a larger error variance of $(10 \text{ dB})^2$ is specified within the EnKF assimilation for reflectivity, in an attempt to reflect the larger attenuation-related error in the data. We note here that the $(10 \text{ dB})^2$ is not intended to be a precise estimate of the actual error including attenuation, but a rough guess for testing the impact. In practice, attenuation correction should be performed one way or another.

As mentioned earlier, we performed additional sensitivity experiments where observations are simulated using formulations and/or parameters that are different from those in the observation operators used during data assimilation. Here the differences include the use of T-matrix instead of Mie scattering calculations, and the use of rainwater, snow, and hail intercept parameters that are half or twice of their default values, and the rainwater intercept parameter diagnosed from rainwater content W (Equation (12), Table I and Figure 1 in Zhang *et al.*, 2008). Such data are assimilated the same way as in earlier experiments, assuming Mie scattering and default values of N_{0r} , N_{0s} , and N_{0h} in the observation operator. We perform the experiments using Z data only, and using both Z and V_r data. These experiments are named ACZhalf, ACZVhalf, ACZdouble, ACZVdouble, ACZdiagN0r, and ACZVdiagN0r (Table II). This serves to test the robustness of our assimilation and attenuation correction procedure in the presence of observation operator error, and in particular error due to DSD uncertainties. Finally, we test the effect of systematic radar calibration error that has the potential to break the attenuation correction through error accumulation; we perform experiments ACZ1dB and ACZV1dB in which 1 dB constant error is added to all attenuated reflectivity observations while the assimilation system assumes the same unbiased 2 dB error observation error standard deviation (Table II). The results of these experiments are presented next.

Table II. List of experiments.

Experiment	Observations	Observations assimilated	Attenuation correction	Observation error	N_{0r} , N_{0r} , N_{0r} , in observation simulation
NAZV	No attenuation	Z and V_r	N.A.	Gaussian	default
NAZ	No attenuation	Z	N.A.	Gaussian	default
ACZV	Attenuated	Z and V_r	Yes	Gaussian	default
ACZ	Attenuated	Z	Yes	Gaussian	default
NACZV	Attenuated	Z and V_r	No	Gaussian	default
NACZ	Attenuated	Z	No	Gaussian	default
NACLEZV	Attenuated	Z and V_r	No	Gaussian	default
NACLEZ	Attenuated	Z	No	Gaussian	default
ACZhalf	Attenuated	Z	Yes	Gaussian	halved
ACZdouble	Attenuated	Z	Yes	Gaussian	doubled
ACZdiagN0r	Attenuated	Z	Yes	Gaussian	diagnosed
ACZ1dB	Attenuated	Z	Yes	Gaussian + 1dB	default
ACZVhalf	Attenuated	Z and V_r	Yes	Gaussian	halved
ACZVdouble	Attenuated	Z and V_r	Yes	Gaussian	doubled
ACZVdiagN0r	Attenuated	Z and V_r	Yes	Gaussian	diagnosed
ACZV1dB	Attenuated	Z and V_r	Yes	Gaussian + 1dB	default

4. Results of experiments

Similar to our earlier papers, we examine the quality of state estimation, i.e. the analyzed individual model state variables by looking at the root-mean-square (RMS) errors of ensemble mean analyses during the analysis cycles. As in our earlier papers, these RMS errors are calculated against the truth fields in regions where the truth reflectivity is greater than 10 dBZ only, i.e. the verification is performed for storm-scale features. For clarity, we show the RMS errors for the analyses only, not for the background forecasts.

Figure 3 compares the RMS errors from the first set of four standard experiments (NAZ, ACZ, NACZ, and NACLEZ) that assimilate reflectivity data only, while Figure 4 compares the errors for NAZV, ACZV, NACZV, and NACLEZV that assimilate both Z and V_r data. Similar to the results of our earlier studies (TX05 and XTD06) without attenuation, the ensemble mean analysis RMS errors of NAZ and NAZV (thick solid curves in Figure 3 and 4) are very low during the later cycles for all state variables. For example, the errors of u and v are less than 1 m s^{-1} , that of w is below 0.5 m s^{-1} and those of hydrometeors are close to or below 0.05 g kg^{-1} . Between them, the errors of NAVZ, with the help of V_r data, are consistently lower than those of NAZ, particularly in earlier cycles.

It can be seen that when attenuated data are assimilated in NACZ and NACZV as if they were not attenuated, the analysis errors (thin dashed curves in Figure 3 and 4) are rather large, especially during later data assimilation cycles when attenuation is more severe with large hydrometeor production in the storm system. The errors of u and v remain above 1.5 m s^{-1} throughout the period and are significantly above 2 m s^{-1} at the end of assimilation. The errors of hydrometeor fields are many times larger than those of corresponding cases

without attenuation or with attenuation correction. It is also interesting to note that the errors of NACZV are in general only slightly lower than those of NACZ, despite the inclusion of V_r data. This indicates a significant negative impact from using attenuated reflectivity data when no correction is applied, even when good V_r data are available.

In ACZ and ACZV, the attenuated data are assimilated with the attenuation correction procedure applied, the error levels of all variables (thick dashed curves in Figure 3 and 4) during the intermediate and later cycles are in fact very close to those of the corresponding cases without attenuation at all (thick solid curves), indicating that the attenuation correction procedure works very effectively. There is more difference in early cycles between the cases with attenuation correction and those with no attenuation at all, because at this time the state estimation is poor, thus attenuation calculations based on the estimated state are not very accurate either.

In NACZ and NACZV, the error variance specified for the attenuated reflectivity data still has a low value of $(2 \text{ dB})^2$, which is actually too low when the attenuation is part of the reflectivity error, i.e. when its effect is not accounted for in the observation operator. In NACLEZ and NACLEZV, this error variance is increased to a more appropriate value of $(10 \text{ dB})^2$ to reflect larger errors in the presence of attenuation but without correction. It turns out that the analyses of NACLEZ (thin solid curves in Figure 3) are significantly worse than those of NACZ (thin dashed curves in Figure 3), particularly in later cycles. Apparently, when only reflectivity is assimilated, specifying a rather larger error variance for the reflectivity data further decreases the constraint of the observations on the model solution, resulting in worse storm analyses. When a larger error variance of $(10 \text{ dB})^2$ is specified for the reflectivity data in NACLEZV (thin solid curves, Figure 4), the analyses are noticeably improved over

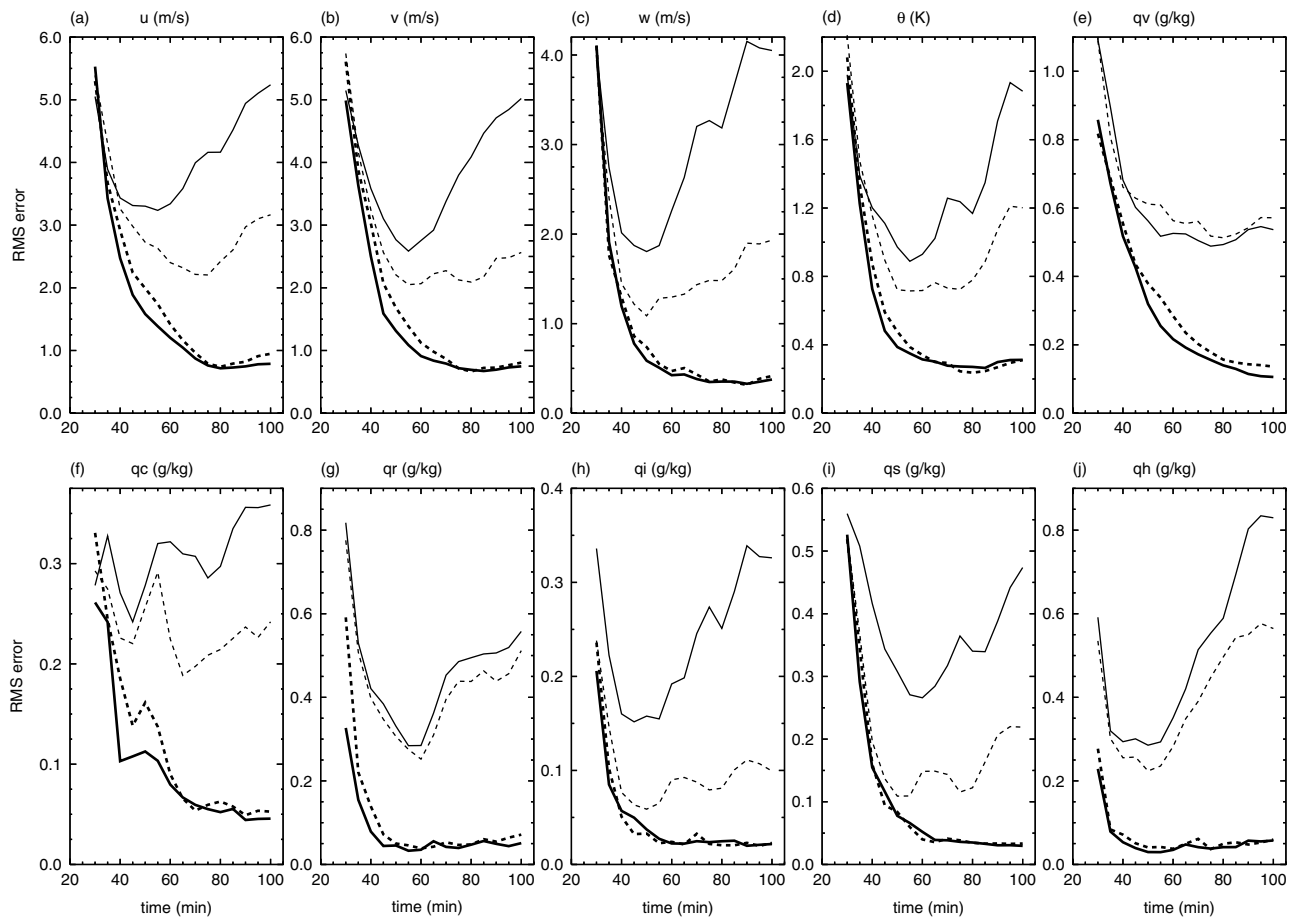


Figure 3. Ensemble mean analysis RMS errors averaged over points where true Z is greater than 10 dBZ for (a) u , (b) v , (c) w , (d) θ , (e) q_v , (f) q_c , (g) q_r , (h) q_i , (i) q_s , and (j) q_h , for experiments NAZ (thick solid), ACZ (thick dashed), NACZ (thin dashed) and NACLEZ (thin solid). Units are shown in the plots.

those of NACZV (thin dashed curves, Figure 4) during later cycles, rather than becoming worse as in NACLEZ. Apparently, reflectivity data receive a reduced weight in the assimilation in this case, allowing high-quality V_r data to have a larger positive impact.

The above findings are further corroborated by the comparison of analyzed low-level model fields (θ' associated with cold pool, reflectivity Z and perturbation wind vectors) shown in Figure 5 at the end of assimilation (100 min). Immediately clear is that the analyses of ACZ and ACZV (Figure 5(d) and (h)) with attenuation correction are very close to the truth (a), while those of NACZ and NACZV (Figure 5(b) and (f)) are similarly poor, with reflectivity patterns similar to those of attenuated truth in Figure 5(e). There are clear differences in the analyzed wind fields of these two runs from truth, although NACZV is better due to the inclusion of V_r data.

When a large error variance is specified for reflectivity data in NACLEZV (Figure 5(g)), the analysis is much better than that of NACZV, due to the increased impact of V_r data. In fact, despite the use of attenuated reflectivity data without correction in NACLEZV, the analyzed reflectivity field looks closer to the truth in Figure 5(a) than to the attenuated truth in Figure 5(e). The analysis of NACLEZ is the worst among all experiments; in this case the impact of available attenuated reflectivity data

is further reduced by large specified error. The analyzed cold pool is the weakest in this case (Figure 5(c)) while that of NACLEZV is rather good (Figure 5(g)).

Figure 6 plots the RMS errors from ACZhalf, ACZdouble and ACZdiagN0r that include effective DSD-related reflectivity observation operator error, and those of ACZ1dB that include a constant 1 dB radar calibration error in reflectivity. Also plotted are the error curves from NAZ and NACZ for reference. It can be seen that, despite the error in the reflectivity observation operator that affects reflectivity and attenuation calculations, the analysis error levels of ACZhalf, ACZdouble and ACZdiagN0r are all very close to those of NAZ that has a perfect observation operator and no attenuation. The error level of ACZdiagN0r is the largest among the three, which is consistent with the fact that the reflectivity and attenuation curves differ more from those of Mie scattering calculation with default N_{0r} . Overall, their error levels are much lower than those of NACZV, where no attenuation correct was performed. The analysis in the presence of an additional 1 dB constant calibration error, from experiment ACZ1dB, also has error levels that are very close to those of NAZ, indicating the robustness of our attenuation correction algorithm to systematic error. We note that these results are obtained without the assistance of V_r data in this case; i.e. the state estimation of the storm

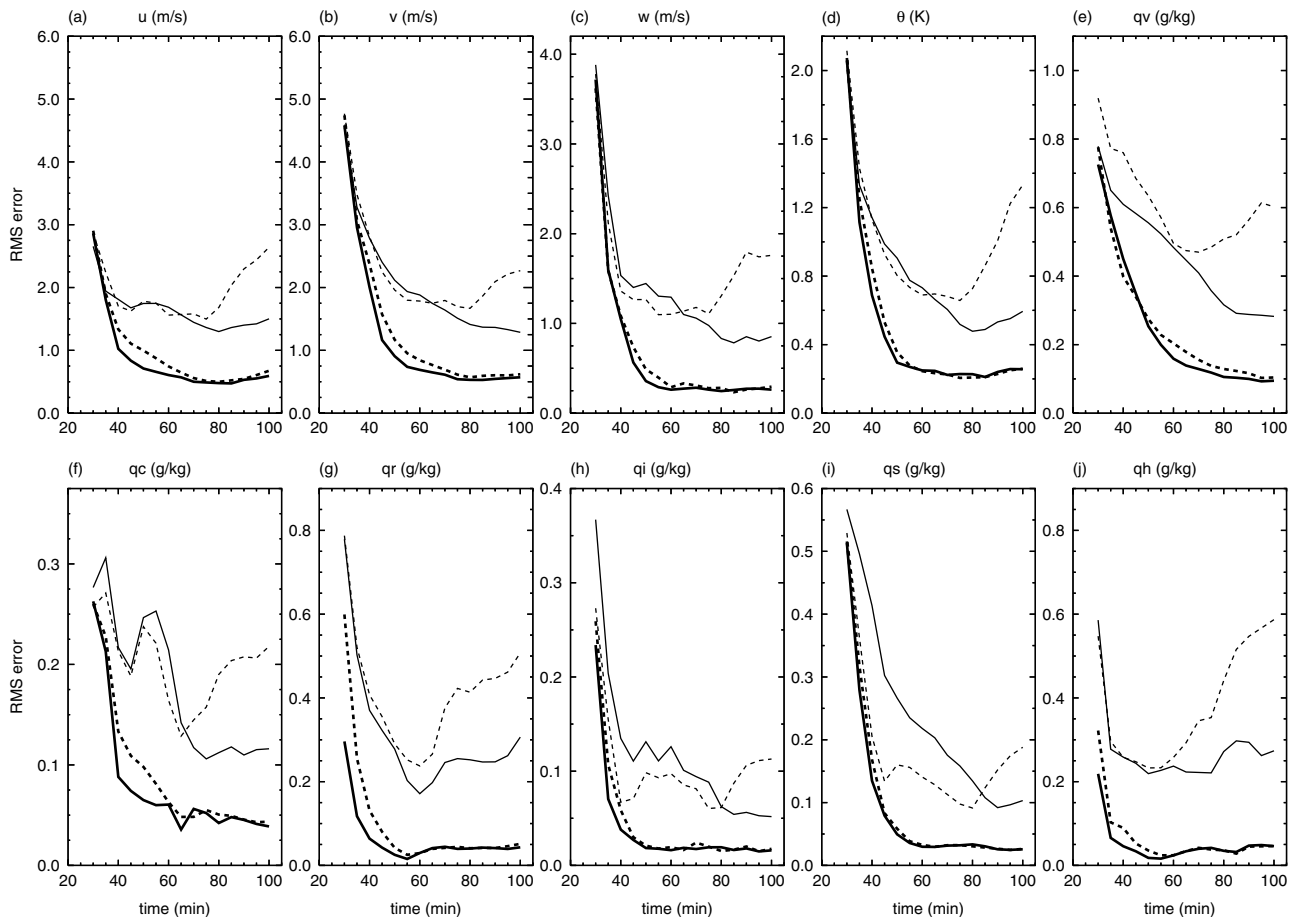


Figure 4. As Figure 3, but for experiments NAZV (thick solid), ACZV (thick dashed), NACZV (thin dashed) and NACLEZV (thin solid).

relied completely on the attenuated reflectivity data. The attenuation correction has to be effective for the state estimation to be successful.

The next set of experiments parallels those just reported, except for the inclusion of V_r data, which are not affected by reflectivity attenuation in our experiments. With the help of additional V_r data, the analysis results are improved over the already excellent results. For example, at the end of the assimilation, u RMS error is about 1 m s^{-1} in ACZVdiagN0r while that in ACZdiagN0r is about 1.5 m s^{-1} (Figure 7). Similar relative differences can be found in the errors of v , q_v , and q_c .

For those who are interested in precipitation estimate, the error in q_r is most relevant. We note that at the end of assimilation cycles, the RMS errors of q_r in the cases with observation operator or radar calibration error are no more than 0.05 g kg^{-1} greater than those of no attenuation cases. Assuming that such an error persists over one hour, and near-surface q_r is about 15 g kg^{-1} , and rainwater falls at about 8 m s^{-1} , the accumulated rainfall error over one hour will be about 2 mm, a rather small error.

The results of the above experiments indicate that our attenuation correction procedure as part of the EnKF data assimilation system is robust and appears to be much less sensitive to DSD model or radar calibration error than conventional methods. The ability of an EnKF system to make use of information from multiple sources,

including information on their error, is believed to be a key distinguishing factor.

5. Summary

In this article, we examined an alternative approach to dealing with attenuation in short-wavelength radar reflectivity data, when they are used to initialize storm-scale NWP models. Unlike the traditional approach, where attenuation correction is performed in observation space before assimilating data into NWP models, we build the attenuation effect into the data assimilation system by calculating the expected attenuation within the forward observation operators. The attenuation is based on the current *estimate* of the atmospheric state, including the hydrometeor species. The estimated state is obtained through an ensemble-based data assimilation system, using *attenuated* data. For this reason, we perform simultaneous attenuation correction and state estimation. Such a procedure has similar advantages to those discussed by Hogan (2007) in his variational procedure for precipitation estimation from attenuated radar data. Our procedure does not require any prior assumption about the specific hydrometeor types at particular grid points (in fact, it allows for mixed types at any grid point) and it is possible to include error or uncertainty from all sources of information in the assimilation framework

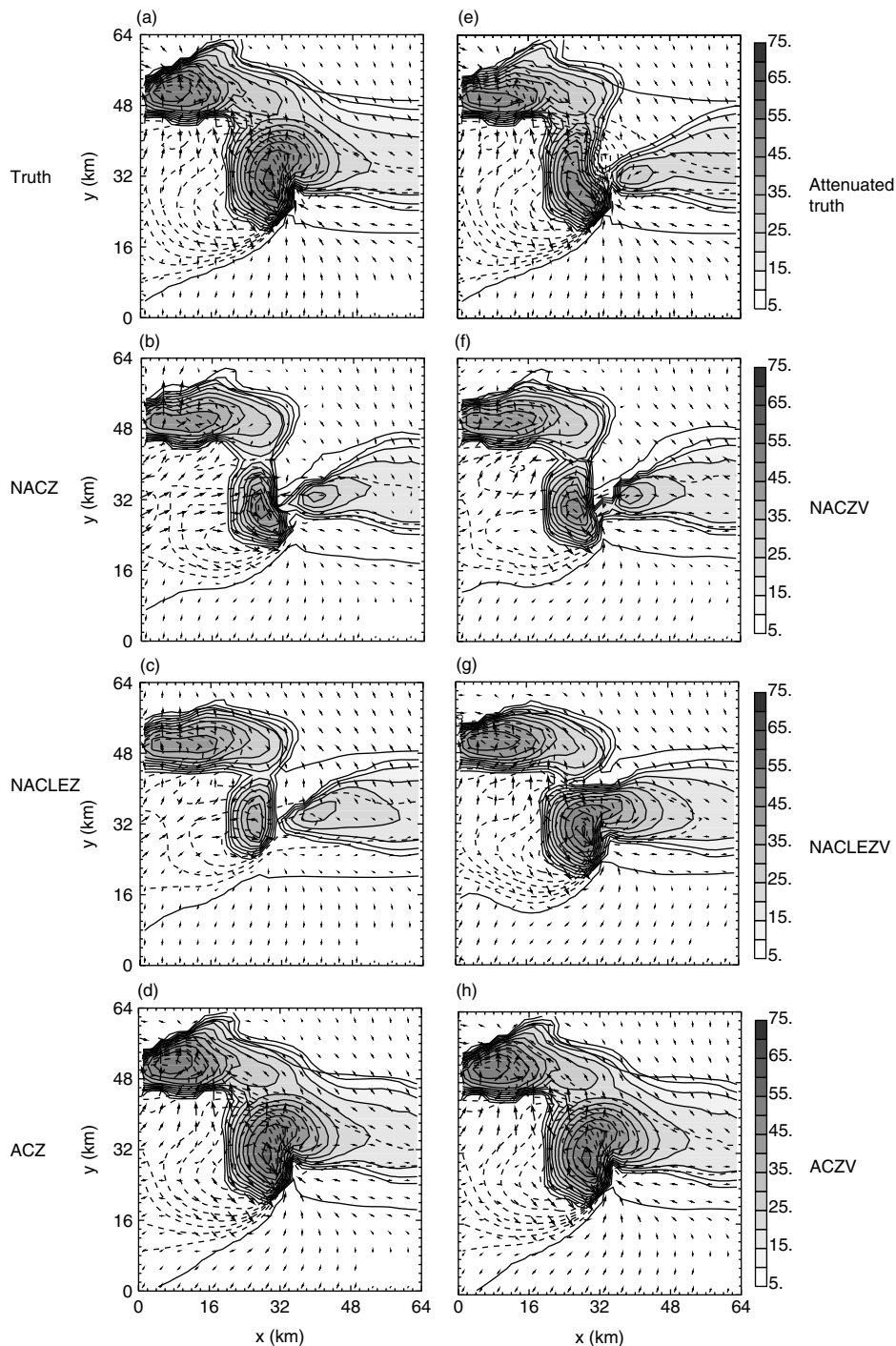


Figure 5. Perturbation wind (vectors; m s^{-1}), perturbation θ (thick black lines for 0 K and thin dashed contours at 0.5 K intervals) and computed Z (thin solid contours and shading at intervals of 5 dB) at $z = 250$ m of (a) the truth simulation, (e) attenuated truth, and ensemble mean analyses from experiments labeled in the figure, at 100 min (the end of assimilation).

and to allow for a close coupling of attenuation correction with the dynamic model. As the model state estimation improves through data assimilation, the estimate and correction of attenuation also improve. With traditional observation-based methods, dual-polarization or dual-frequency measurements have to be available in order to infer any information about the DSD or hydrometeor species. In this study, only single-polarization reflectivity data are assumed available, while some experiments assume the availability of additional radial velocity data.

The effectiveness of our procedure is demonstrated using a set of observing system simulation experiments (OSSEs), in this proof-of-concept study, the first of its kind. Simulated radar observations are first collected from a model-simulated supercell thunderstorm using a radar emulator. The simulated data show complete attenuation of X-band reflectivity behind the precipitation core of the supercell. Without attenuation correction, the analyzed storm and precipitation core are much weaker. The RMS errors of the analyzed model fields are 4 to 10 times larger

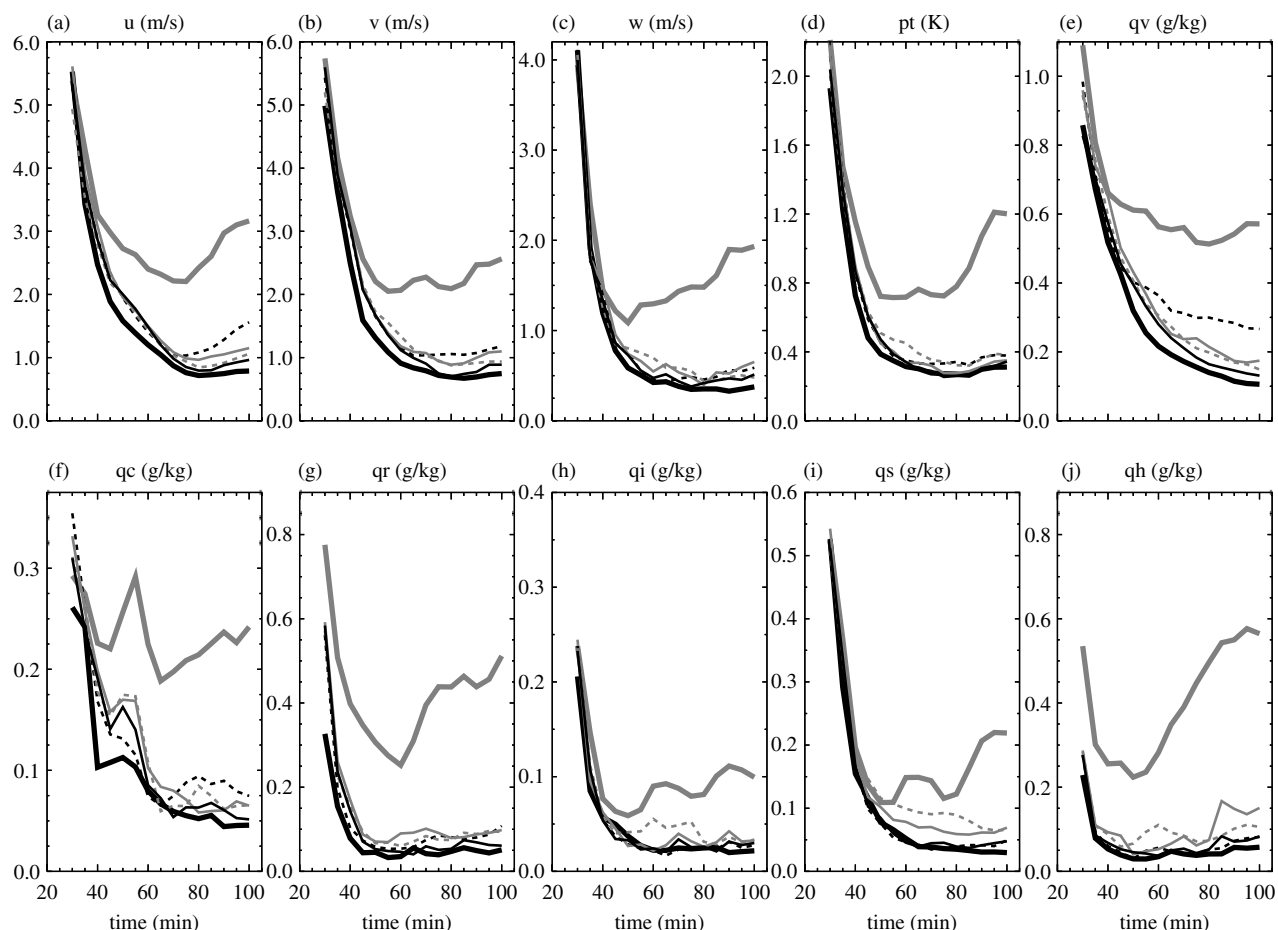


Figure 6. As Figure 3, but for experiment NACZ (thick grey), NAZ (thick black), ACZ1dB (thin solid black), ACZdiagN0r (thin dashed black), ACZhalf (thin solid grey), and ACZdouble (thin dashed grey).

than those of the baseline case using unattenuated data. With our procedure of simultaneous state estimation and attenuation correction, the analysis obtained is almost as good as the corresponding case with no attenuation. It is also shown that, when high-quality radial velocity data are assimilated together with attenuated reflectivity data, the attenuation in the reflectivity data still has a similar negative impact on the analysis if the attenuation effect is not included in the observation operator. When the reflectivity data are weighted less by specifying a larger error variance, the negative impact is reduced if radial velocity data are also assimilated, but is further increased if only reflectivity data are available. In the latter case, the available reflectivity data become even less effective because of their reduced weight in the assimilation system relative to the background or prior estimate.

The robustness of our attenuation correction procedure was further tested by introducing significant error to the rain, snow and hail intercept parameters that are involved in the reflectivity and attenuation calculations. It was shown that when the parameters were halved or doubled, or when a diagnostic formula for the rain intercept parameter was used instead in the data generation while the original observation operator is used in the data assimilation, the analyses are still very successful. Neglecting the effect of non-spherical raindrop shapes in

the observation operator is found to have minimal impact. Further, the procedure is not sensitive to moderate-sized systematic radar calibration error.

Still, our procedure assumes some knowledge about the DSDs of the hydrometeors, even though it does not need to know, *a priori*, the composition of hydrometeors at each grid cell. Our recent study (Tong and Xue, 2008a) has shown that it is possible to estimate uncertain DSD-related parameters through simultaneous state and parameter estimation with the EnKF method. Simultaneous state and parameter estimation, together with attenuation correction, where the uncertain parameters to be estimated are involved in the reflectivity and attenuation calculations, are interesting research topics for the future. The use and benefit of additional polarimetric radar data in such a setting should be investigated. Our recent study that includes the effect of DSD parameters in reflectivity calculations has shown encouraging results (Jung *et al.*, 2009). We also plan to apply this new approach to real X-band observations collected in the CASA project, and compare the results against traditional attenuation correction methods. Given the general challenges facing storm-scale data assimilation using radar data, much research is still needed in these areas. Because there are many possible sources of uncertainty, experimentation using simulated data is a natural first step for testing

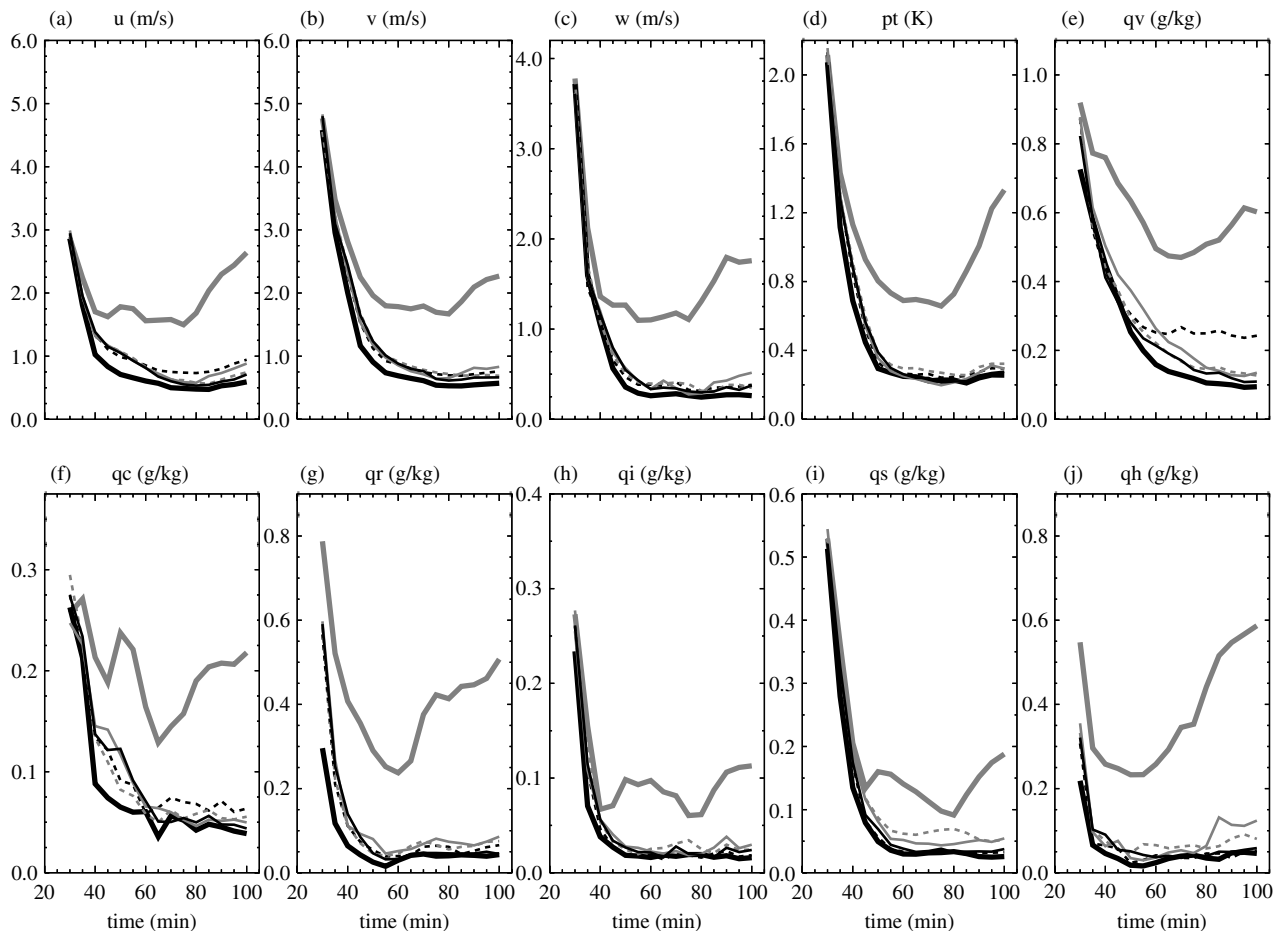


Figure 7. As Figure 3, but for experiment NACZV (thick grey), NAZV (thick black), ACZV1dB (thin solid black), ACZVdiagN0r (thin dashed black), ACZVhalf (thin solid grey), and ACZVdouble (thin dashed grey).

a new approach and its value should not be discounted. Finally, we point out that in our procedure, the end products are the analyses of the three-dimensional fields of hydrometeors and all other model state variables; this task is generally much more challenging than estimating two-dimensional reflectivity or rain-rate fields as is typically the case in quantitative precipitation estimation studies.

Acknowledgements

This work was primarily supported by NSF grants EEC-0313747, ATM-0530814 and ATM-0608168 and grant KLME060203 from Nanjing University of Information Science and Technology. Computations were performed at the Pittsburgh Supercomputing Center. Nathan Snook is thanked for proofreading the manuscript.

References

- Anagnostou MN, Anagnostou EN, Vivekanandan J. 2006. Correction for rain path specific and differential attenuation of X-band dual-polarization observations. *IEEE Trans. Geosci. Remote Sensing* **44**: 2470–2480.
- Brandes EA, Zhang G, Vivekanandan J. 2002. Experiments in rainfall estimation with a polarimetric radar in a subtropical environment. *J. Appl. Meteorol.* **41**: 674–685.
- Bringi VN, Chandrasekar V. 2000. *Polarimetric Doppler Weather Radar*. Cambridge University Press.
- Bringi VN, Keenan TD, Chandrasekar V. 2001. Correcting C-band radar reflectivity and differential reflectivity data for rain attenuation: A self-consistent method with constraints. *IEEE Trans. Geosci. Remote Sensing* **39**: 1906–1915.
- Daley R. 1991. *Atmospheric Data Analysis*. Cambridge University Press.
- Dawson DT, II, Xue M, Milbrandt JA, Yau MK. 2009. The effects of evaporation and melting in a multi-moment bulk microphysics scheme on the low-level downdrafts and surface cold pools in the simulations of the 3 May 1999 Oklahoma tornadic thunderstorms. *Mon. Weather Rev.* submitted.
- Doviak R, Zrnic D. 1993. *Doppler Radar and Weather Observations*. Academic Press.
- Evensen G. 1994. Sequential data assimilation with a nonlinear quasi-geostrophic model using Monte Carlo methods to forecast error statistics. *J. Geophys. Res.* **99**: 10143–10162.
- Gao J, Brewster K, Xue M. 2006. A comparison of the radar ray path equations and approximations for use in radar data assimilation. *Adv. Atmos. Sci.* **23**: 190–198.
- Hitschfeld W, Bordan J. 1954. Errors inherent in the radar measurement of rainfall at attenuating wavelengths. *J. Meteorol.* **11**: 58–67.
- Hogan RJ. 2007. A variational scheme for retrieving rainfall rate and hail reflectivity fraction from polarization radar. *J. Appl. Meteorol. Climatol.* **46**: 1544–1564.
- Hong S-Y, Lim J-OJ. 2006. The WRF single-moment 6-class microphysics scheme (WSM6). *J. Korean Meteorol. Soc.* **42**: 129–151.
- Hu M, Xue M, Brewster K. 2006a. 3DVAR and cloud analysis with WSR-88D level-II data for the prediction of Fort Worth tornadic thunderstorms. Part I: Cloud analysis and its impact. *Mon. Weather Rev.* **134**: 675–698.
- Hu M, Xue M, Gao J, Brewster K. 2006b. 3DVAR and cloud analysis with WSR-88D level-II data for the prediction of Fort Worth tornadic

- thunderstorms. Part II: Impact of radial velocity analysis via 3DVAR. *Mon. Weather Rev.* **134**: 699–721.
- Jameson A. 1992. The effect of temperature on attenuation-correction schemes in rain using polarization propagation differential phase shift. *J. Appl. Meteorol.* **31**: 1106–1118.
- Johnson B, Brandes EA. 1987. Attenuation of a 5-cm wavelength radar signal in the Lahoma-Oriente storms. *J. Atmos. Oceanic Technol.* **4**: 512–517.
- Jung Y, Zhang G, Xue M. 2008. Assimilation of simulated polarimetric radar data for a convective storm using ensemble Kalman filter. Part I: Observation operators for reflectivity and polarimetric variables. *Mon. Weather Rev.* **136**: 2228–2245.
- Jung Y, Xue M, Zhang G. 2009. Simultaneous estimation of microphysical parameters and atmospheric state using simulated polarimetric radar data and ensemble Kalman filter in the presence of observation operator error. *Mon. Weather Rev.* submitted.
- Kalnay E. 2002. *Atmospheric Modeling, Data Assimilation, and Predictability*. Cambridge University Press.
- Lin Y-L, Farley RD, Orville HD. 1983. Bulk parameterization of the snow field in a cloud model. *J. Climatol. Appl. Meteorol.* **22**: 1065–1092.
- Lord SJ, Kalnay E, Daley R, Emmitt GD, Atlas R. 1997. 'Using OSSEs in the design of the future generation of integrated observing systems'. Pp 45–47 in preprints for First Symposium on Integrated Observation Systems, Long Beach, CA. Amer. Meteorol. Soc: Boston.
- Matrosov SY, Clark KA, Martner BE, Tokay A. 2002. X-band polarimetric radar measurements of rainfall. *J. Appl. Meteorol.* **41**: 941–952.
- McLaughlin D, Knapp E, Wang Y, Chandrasakar V. 2007. 'Short wavelength technology and the potential for distributed networks of small radar systems'. *IEEE Radar 2007 Conference Digest*.
- Meneghini R, Kozu T. 1990. *Space-borne Weather Radar*. Artech House: Boston.
- Meneghini R, Liao L. 2007. On the equivalence of dual-wavelength and dual-polarization equations for estimation of the raindrop size distribution. *J. Atmos. Oceanic Technol.* **24**: 806–820.
- Milbrandt JA, Yau MK. 2005. A multi-moment bulk microphysics parameterization. Part II: A proposed three-moment closure and scheme description. *J. Atmos. Sci.* **62**: 3065–3081.
- Milbrandt JA, Yau MK. 2006. A multimoment bulk microphysics parameterization. Part III: Control simulation of a hailstorm. *J. Atmos. Sci.* **63**: 3114–3136.
- Park SG, Bringi VN, Chandrasekar V, Maki M, Iwanami K. 2005. Correction of Radar Reflectivity and Differential Reflectivity for Rain Attenuation at X Band. Part I: Theoretical and Empirical Basis. *J. Atmos. Oceanic Technol.* **22**: 1621–1632.
- Ray PS. 1972. Broadband complex refractive indices of ice and water. *Appl. Opt.* **11**: 1836–1844.
- Ray PS, Johnson B, Johnson KW, Bradberry JS, Stephens JJ, Wagner KK, Wilhelmson RB, Klemp JB. 1981. The morphology of severe tornadic storms on 20 May 1977. *J. Atmos. Sci.* **38**: 1643–1663.
- Ryzhkov A, Zrnic DS. 1995. Precipitation and attenuation measurements at a 10-cm wavelength. *J. Appl. Meteorol.* **34**: 2121–2134.
- Smyth TJ, Illingworth AJ. 1998. Correction for attenuation of radar reflectivity using polarization data. *Q. J. R. Meteorol. Soc.* **124**: 2393–2415.
- Snyder C, Zhang F. 2003. Assimilation of simulated Doppler radar observations with an ensemble Kalman filter. *Mon. Weather Rev.* **131**: 1663–1677.
- Sun J, Crook NA. 1997. Dynamical and microphysical retrieval from Doppler radar observations using a cloud model and its adjoint. Part I: Model development and simulated data experiments. *J. Atmos. Sci.* **54**: 1642–1661.
- Tong M, Xue M. 2005. Ensemble Kalman filter assimilation of Doppler radar data with a compressible nonhydrostatic model: OSS Experiments. *Mon. Weather Rev.* **133**: 1789–1807.
- Tong M, Xue M. 2008a. Simultaneous estimation of microphysical parameters and atmospheric state with radar data and ensemble square-root Kalman filter. Part II: Parameter estimation experiments. *Mon. Weather Rev.* **136**: 1649–1668.
- Tong M, Xue M. 2008b. Simultaneous estimation of microphysical parameters and atmospheric state with radar data and ensemble square-root Kalman filter. Part I: Sensitivity analysis and parameter identifiability. *Mon. Weather Rev.* **136**: 1630–1648.
- Whitaker JS, Hamill TM. 2002. Ensemble data assimilation without perturbed observations. *Mon. Weather Rev.* **130**: 1913–1924.
- Xue M, Droegemeier KK, Wong V. 2000. The Advanced Regional Prediction System (ARPS) – A multiscale nonhydrostatic atmospheric simulation and prediction tool. Part I: Model dynamics and verification. *Meteorol. Atmos. Phys.* **75**: 161–193.
- Xue M, Tong M, Droegemeier KK. 2006. An OSSE framework based on the ensemble square-root Kalman filter for evaluating impact of data from radar networks on thunderstorm analysis and forecast. *J. Atmos. Oceanic Technol.* **23**: 46–66.
- Xue M, Liu S, Yu T. 2007a. Variational analysis of over-sampled dual-Doppler radial velocity data and application to the analysis of tornado circulations. *J. Atmos. Oceanic Technol.* **24**: 403–414.
- Xue M, Jung Y, Zhang G. 2007b. Error modeling of simulated reflectivity observations for ensemble Kalman filter data assimilation of convective storms. *Geophys. Res. Lett.* **34**: L10802, DOI:10.1029/2007GL029945.
- Xue M, Wang D-H, Gao J-D, Brewster K, Droegemeier KK. 2003. The Advanced Regional Prediction System (ARPS), storm-scale numerical weather prediction and data assimilation. *Meteorol. Atmos. Phys.* **82**: 139–170.
- Xue M, Droegemeier KK, Wong V, Shapiro A, Brewster K, Carr F, Weber D, Liu Y, Wang D-H. 2001. The Advanced Regional Prediction System (ARPS) – A multiscale nonhydrostatic atmospheric simulation and prediction tool. Part II: Model physics and applications. *Meteorol. Atmos. Phys.* **76**: 143–165.
- Zhang G, Vivekanandan J, Brandes E. 2001. A method for estimating rain rate and drop size distribution from polarimetric radar measurements. *IEEE Trans. Geosci. Remote Sens.* **39**: 830–841.
- Zhang G, Xue M, Cao Q, Dawson D. 2008. Diagnosing the intercept parameter for exponential raindrop size distribution based on video disdrometer observations. *J. Appl. Meteorol. Climatol.* **47**: 2983–2992.